



Bayesian optimization of entropy-stabilized metal fluoride conversion cathodes and their synthesis

Aditya Sundar^a, Jehee Park^{b,d}, Haesun Park^{a,c}, Eungje Lee^d, Jae Jin Kim^d, Peter Zapol^{a,*}

^a Materials Science Division, Argonne National Laboratory, 9700 S. Cass Avenue, Lemont, IL, 60439, USA

^b Department of Chemical and Biological Engineering, Hanbat National University, Yuseong-Gu, Daejeon, 34158, Republic of Korea

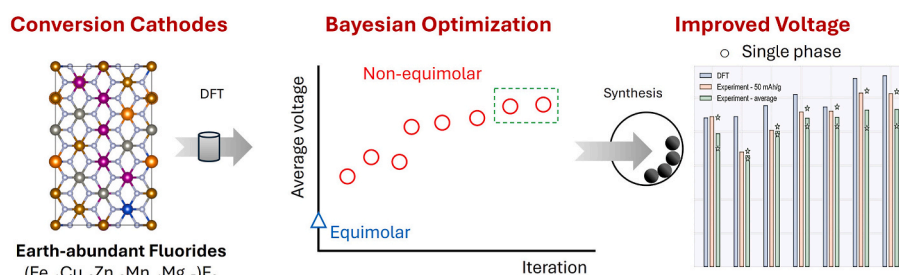
^c School of Integrative Engineering, Chung-Ang University, Seoul, 06974, Republic of Korea

^d Chemical Sciences and Engineering Division, Argonne National Laboratory, 9700 S. Cass Avenue, Lemont, IL, 60439, USA

HIGHLIGHTS

- Bayesian optimization of high entropy earth abundant fluoride cathodes for sustainable battery.
- Theoretical voltage, free energy, and electronic structure of non-equimolar compositions from density functional theory.
- Synthesis of predicted non-equimolar quinary Co and Ni free fluorides improved conversion reaction voltage by up to 28 %.
- Non-equimolar compositions with cycling stability superior to known multi-element fluorides were found.

GRAPHICAL ABSTRACT



ARTICLE INFO

Keywords:

High-entropy alloy
Bayesian optimization
Conversion cathode
Fluoride

ABSTRACT

Fluoride-based conversion cathodes are promising for next-generation Li ion batteries because of their high voltage and energy densities. High entropy earth abundant fluoride cathodes are attractive for sustainable battery because of the potentially higher cycling stability. While Ni and Co containing equimolar alloys stabilized by high entropy were considered previously, Ni and Co free non-equimolar metal alloy compositions might offer new opportunities to increase materials stability and average voltage. This opportunity was pursued using Bayesian optimization of average voltage for the computational prediction of $(\text{Fe}_{x1}\text{Cu}_{x2}\text{Zn}_{x3}\text{Mn}_{x4}\text{Mg}_{x5})\text{F}_2$ cathode chemistries. Theoretical voltage, room temperature free energy, and electronic structure of potentially high voltage compositions were computed using density functional theory calculations. The experimental realization of non-equimolar quinary Co and Ni free fluorides with stable rutile single phase and improved conversion reaction voltage by up to 28 % compared to the equimolar alloy demonstrated the power of Bayesian optimization methods for the computationally guided experimental synthesis of fluoride cathodes. Finally, non-equimolar cathode chemistries were found with cycling stability superior to known multi-element fluorides.

* Corresponding author.

E-mail address: zapol@anl.gov (P. Zapol).

<https://doi.org/10.1016/j.jpowsour.2025.236448>

Received 7 May 2024; Received in revised form 14 October 2024; Accepted 31 January 2025

Available online 16 February 2025

0378-7753/© 2025 UChicago Argonne LLC. Published by Elsevier B.V. This is an open access article under the CC BY-NC-ND license (<http://creativecommons.org/licenses/by-nc-nd/4.0/>).

1. Introduction

Conversion-type transition metal fluoride cathodes offer several advantages over intercalation-type cathodes in Li-ion batteries, such as multielectron redox reaction (e.g., $\text{FeF}_2 + 2\text{Li} \leftrightarrow \text{Fe} + 2\text{LiF}$) leading to higher energy densities and theoretical capacities and use of earth-abundant non-toxic elements [1–4]. Fluoride cathodes are favored since strongly ionic metal-fluorine bonds result in high redox potentials or conversion reaction voltages [4,5]. However, cycling characteristics of these conversion-type cathodes need to be improved by addressing poor reaction reversibility and volume changes due to phase change [1, 6], particle agglomeration or cracking due to diffusion-limited morphological transformations [7], and blocked ionic conduction pathways due to cathode precipitation and other decomposition reactions [6]. Additionally, these cathodes have reduced electronic conduction arising from the large electronic bandgaps of insulating fluorides [1].

High-entropy multi-element fluoride cathodes present attractive opportunity to improve the electrochemical performance of conversion batteries. High-entropy materials are being actively researched for several applications in energy materials and structural components due to the promise of synergistically enhanced properties resulting in better performance compared to the parent material systems [8–11]. Developing high-entropy fluoride cathodes [12] with multiple transition metal elements may simultaneously result in (i) increased conversion reaction voltages, (ii) thermodynamical stability due to cation-site configurational entropic contributions, and (iii) improved cycling characteristics and decreased hysteresis arising from the balance between various electrochemically active and inactive elements. Such development will improve both gravimetric energy density and cycle life for the cathodes. For instance, CuF_2 cathodes have a high theoretical conversion voltage of 3.55 V with respect to Li/Li^+ (which is the average voltage of the complete conversion reaction calculated using DFT) and capacity of 528 mAh/g [7]. However, Cu agglomeration results in a rapid decrease in discharge capacity after just three cycles [7]. Analogously, while FeF_2 cathodes have a relatively high theoretical conversion reaction voltage of 2.64 V, Fe agglomeration has been shown to result in large voltage hysteresis, up to 2 V, during cycling [6]. Upon Cu alloying to create a solid solution of $\text{Cu}_x\text{Fe}_y\text{F}_2$, the voltage hysteresis was reduced to less than 150 mV [6]. Also, the synergistic redox effect of Cu and Fe was evident in the form of higher conversion reaction voltages and battery capacities compared to a simple 1:1 mixture of FeF_2 and CuF_2 [2,13]. Modification of diffusion pathways was suggested to mitigate hysteresis [6]. Similarly, 25 % Cu substitution in NiF_2 also improved the conversion reaction voltage from 1.35 V to 1.63 V, cycling stability and capacity from 445 mAhg^{-1} to 552 mAhg^{-1} [14]. Recent experimental results on alloyed fluorides containing five, six, and seven metallic elements including Mg (which is electrochemically inactive above 1 V relative to Li/Li^+) showed promising performance with high voltages, capacities, and simultaneously reduced voltage hysteresis [12].

Here, we investigated the performance of non-equimolar $(\text{Fe}_{x1}\text{Cu}_{x2}\text{Zn}_{x3}\text{Mn}_{x4}\text{Mg}_{x5})\text{F}_2$ cathodes in distinction to our previous work, which was focused on equimolar $(\text{X}_{0.2}\text{Cu}_{0.2}\text{Zn}_{0.2}\text{Ni}_{0.2}\text{Co}_{0.2})\text{F}_2$ cathodes (X = Fe, Mg). With the objective of replacing the toxic elements (Ni and Co) with less toxic, earth-abundant and relatively inexpensive Mg and Mn, the goal here was to identify cathode compositions with high conversion voltages compared to the equimolar $(\text{Fe}_{0.2}\text{Cu}_{0.2}\text{Zn}_{0.2}\text{Mn}_{0.2}\text{Mg}_{0.2})\text{F}_2$. The direct use of DFT calculations to investigate the search space in such multi-principal element materials or high-entropy alloys (HEA) is computationally demanding. This bottleneck can be overcome by advanced methods such as graph neural networks and Bayesian Optimization (BO), which have been used for multi-property optimization and accelerated materials discovery [15–17]. Particularly, BO has been demonstrated to be an extremely versatile tool to guide materials design and discovery, both computational [17,18] and experimental [19–21].

For specific examples, BO-based studies on HEA systems have led to (i) DFT-guided experimental discovery of $\text{Ag}_{20}\text{Pd}_{80}$ and $\text{Ir}_{50}\text{Pt}_{50}$ as the most active alloys for electrocatalytic oxygen reduction within the quinary Ag-Ir-Pd-Pt-Ru and Ir-Pd-Pt-Rh-Ru systems after exploring just 150 compositions from a database of more than 10,000 [22], (ii) experimental discovery of $\text{Pt}_{16}\text{Ru}_{46}\text{Pd}_2\text{Rh}_{34}\text{Au}_2$ as the most active catalyst for electrocatalytic H_2/CO oxidation after just 32 experiments within the Pt-Ru-Pd-Rh-Au space [23], (iii) identification of Pareto-optimal alloys within the Mo-Nb-Ti-V-W space with maximized ductility and yield strength for gas turbine applications [24]. Further, regular BO and additive BO (using transfer learning) based DFT calculations were used to screen fast Li and Na ion conductors (energy barrier <0.3 eV) by sampling only ~ 30 % of the chemical space [25].

In this work, we used BO to extract compositions within the $(\text{Fe}_{x1}\text{Cu}_{x2}\text{Zn}_{x3}\text{Mn}_{x4}\text{Mg}_{x5})\text{F}_2$ search space that have high theoretical conversion reaction voltages (high average voltage values), and retain high configurational entropy. The subscripts $x1$, $x2$, $x3$, $x4$, and $x5$ denote the molar fractions in the alloy and sum up to 1. Further, we also report the calculated free energies and electronic structures of these high voltage compositions. Finally, these computational findings were shown to lead to the experimental realization of non-equimolar quinary rutile fluorides with single-phase stability, improved conversion reaction voltages (up to 28 % higher than the equimolar composition) and cycling stability compared to the equimolar fluoride material. This integrated computational-experimental work demonstrated the power of Bayesian Optimization to accelerate battery materials discovery.

2. Results

2.1. Average voltage of the conversion reaction

For binary fluorides, the conversion reaction is given by the following Equation (1a), and its average voltage or redox potential with Li/Li^+ as the reference is calculated using Equation (1b).



$$V = \frac{2E(\text{LiF}_{\text{rocksalt}}) + E(\text{M}) - 2E(\text{Li}_{\text{BCC}}) - E(\text{MF}_{2\text{rutile}})}{2e} \quad 1b$$

where M is Fe, Cu, Zn, Mn, or Mg. The voltage is defined in Equation (1b) as the difference in energies between the reference phases: rocksalt for LiF and rutile for MF_2 per electron charge e . The reference state for Fe was the conventional body-centred cubic (BCC) phase with 2 atoms per unit cell. Mn metal was modeled as α -Mn, which is based on a BCC Bravais lattice with a 29 atom bases. Mg and Zn were modeled as hexagonal close packed (HCP) phases with 2 atoms per conventional cell. Cu was modeled as a conventional face-centred cubic (FCC) phase with 4 atoms per cell. The reference state for Li was its metallic BCC phase. Voltages for the conversion reaction were calculated using three different calculation schemes, which differ in the DFT methods used for total energy calculations. The first scheme is using generalized gradient approximation (GGA) for the rutile and metallic phases. The second scheme is using GGA + U for the rutile and metallic phases, where the onsite Coulomb interaction term U is introduced to improve the exchange-correlation energy in strongly correlated systems with d-shell electrons. The third scheme uses a hybrid of GGA and GGA + U, where GGA is used for metallic phases and GGA + U for the fluoride phases, along with a renormalization energy correction [26]. The correction term bridges the GGA and GGA + U calculations by ensuring that the formation enthalpy of the binary fluoride matched the experimental data [27]. The renormalization correction values for FeF_2 , CuF_2 , and MnF_2 were 1.723, 1.156, and 1.687 eV respectively, obtained from Jain et al. [27]. Conversion reaction voltages for binary fluorides obtained using the three calculation schemes and our in-house experiments are shown in Fig. 1(a). These in-house experimental charge-discharge

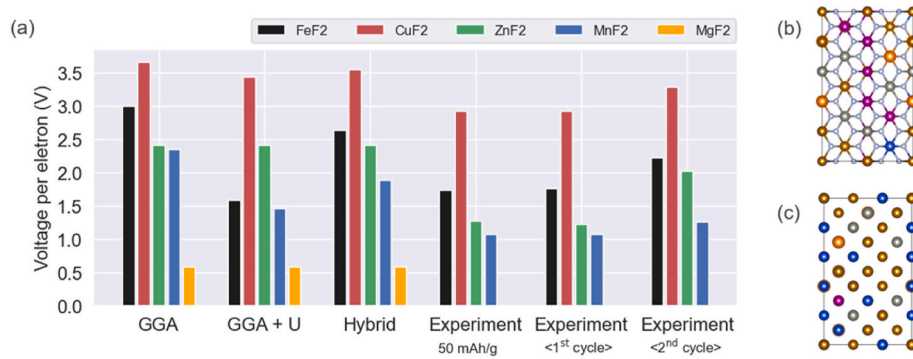
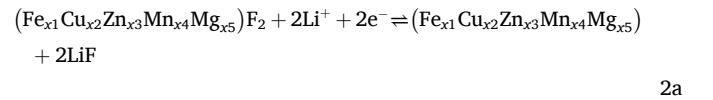


Fig. 1. (a) Comparison of the conversion voltages of single-element fluorides using different methods. The experimental voltages are measured at a specific capacity of 50 mAh/g (fourth set of bar plots) and also by averaging over specific capacities where the voltage profile plateaued (fifth and sixth set of bar plots). (b) Representative atomistic configuration for $(\text{Fe}_{x1}\text{Cu}_{x2}\text{Zn}_{x3}\text{Mn}_{x4}\text{Mg}_{x5})\text{F}_{2(\text{rutile})}$, (c) representative atomistic configuration for $(\text{Fe}_{x1}\text{Cu}_{x2}\text{Zn}_{x3}\text{Mn}_{x4}\text{Mg}_{x5})_{\text{BCC}}$. Different colors denote different metallic elements. The small silver atoms in (b) denote F atoms. (For interpretation of the references to color in this figure legend, the reader is referred to the Web version of this article.)

profiles are presented in Fig. S1 and Table S1 of the Supplementary Information (SI).

While the GGA method captured the experimental voltage trend for FeF₂, CuF₂, and ZnF₂, it was inherently inaccurate for transition metal fluorides since it does not include any on-site interaction energies. Including these energies using the GGA + U formulation for both rutile and metallic phases did not capture the experimental trend. In a benchmark study, computational voltages for CuF₂, NiF₂, and FeF₂ using the hybrid mixing scheme was reported to close match the Gibbs free

Analogous to Equations (1a) and (1b), Equations (2a) and (2b) define the conversion reaction for multi-element fluorides.



$$V = \frac{2E(\text{LiF}_{\text{rocksalt}}) + E(\text{Fe}_{x1}\text{Cu}_{x2}\text{Zn}_{x3}\text{Mn}_{x4}\text{Mg}_{x5}) - 2E(\text{Li}_{\text{BCC}}) - E(\text{Fe}_{x1}\text{Cu}_{x2}\text{Zn}_{x3}\text{Mn}_{x4}\text{Mg}_{x5}\text{F}_{2\text{rutile}})}{2|e|} \quad (2b)$$

energy of formation of these fluorides from standard thermodynamic tables [26]. Therefore, the hybrid scheme was used in this study and was found to give qualitatively consistent results with experimental conversion voltages for FeF₂, CuF₂, ZnF₂, and MnF₂. Since MgF₂ is not electrochemically active for the conversion reaction above 1 V vs Li/Li⁺, experimental voltage values are not reported for MgF₂ cathodes. We also note the relatively good agreement between voltages calculated using the GGA and hybrid schemes from Fig. 1(a). While values for MgF₂ and ZnF₂ were unchanged from the GGA values, CuF₂ voltage was marginally higher (3.3 %), FeF₂ and MnF₂ voltages were moderately higher (13 % and 24 % respectively) relative to the hybrid scheme. Experimental voltages shown in the fourth to sixth sets of bar plots in Fig. 1(a) were obtained using three different protocols. The fourth set of bar plots was obtained at a fixed specific capacity of 50 mAh/g since most of the binary voltage profiles were found to reach a plateau at this capacity (data in the SI). The remaining two sets of experimental voltages were obtained by averaging over a range of specific capacities where the voltage profile has plateaued in the first and second cycle, respectively. It can be noted that for FeF₂, ZnF₂, and MnF₂, the experimental voltages (or redox potential) increased from the first cycle to the second cycle because the kinetic overpotential decreases with the reduction in particle size of the reconverted metal fluorides as activation proceeds during the first cycle [2,6]. On the other hand, CuF₂ showed significantly reduced discharge capacity at the second cycle as its voltage decreases rapidly after small plateau [7]. Analysis details are provided in the SI.

All further results in this manuscript were obtained using the hybrid calculation scheme (GGA for metals, GGA + U for fluorides with a renormalization correction energy). The renormalization energy correction for each high-entropy fluoride was calculated as the composition-weighted sum of the corrections for each binary fluoride.

For simplicity, only the BCC phase was considered for all compositions of the metallic phase $(\text{Fe}_{x1}\text{Cu}_{x2}\text{Zn}_{x3}\text{Mn}_{x4}\text{Mg}_{x5})$. The fractions of metals in the rutile and BCC phases add up to one, i.e. $x1 + x2 + x3 + x4 + x5 = 1$. The energy differences between the BCC and FCC phases of the multiple metallic elements are small and unlikely to change the calculated voltage values by more than 5 mV. The composition of each element was allowed to vary between 0.05 and 0.4 in steps of 0.05, resulting in a total of 2226 compositions of HEF. The upper composition fraction was set to 0.4 since higher fractions of a single element will reduce the contribution of configurational entropy and result in larger deviations from the equimolar composition (refer to Fig. S2 in the SI for details). Fig. 1(b–c) show representative atomistic configurations for the fluoride and metallic phases. Note that the electrochemical inactivity of Mg above 1 V relative to Li/Li⁺ changes the conversion reaction in Equation (2a). The modified chemical reaction is listed in Equation S(1) in the SI. However, this computational study considered complete chemical conversion from the rutile phase to the BCC phase given by Equations (2a) and (2b). Considering Mg inactive would result in a slight increase in average conversion reaction voltage.

We note here that the average voltage for the conversion reaction was chosen as the target property for Bayesian optimization. Additionally, only one SQS configuration was generated per cathode composition. Based on our previous studies, the conversion reaction voltage depends very weakly on the SQS ordering. In contrast, the thermodynamic energy above the convex hull (formation energy) and electronic band gap are much more sensitive to the specific ordering of atoms within SQS. For instance, the standard deviation in the conversion reaction voltage over four SQS configurations for equimolar $(\text{Fe}_{0.2}\text{Cu}_{0.2}\text{Zn}_{0.2}\text{Ni}_{0.2}\text{Co}_{0.2})\text{F}_2$ and $(\text{Mg}_{0.2}\text{Cu}_{0.2}\text{Zn}_{0.2}\text{Ni}_{0.2}\text{Co}_{0.2})\text{F}_2$ was found in our calculations to vary by less than one-hundredth of its

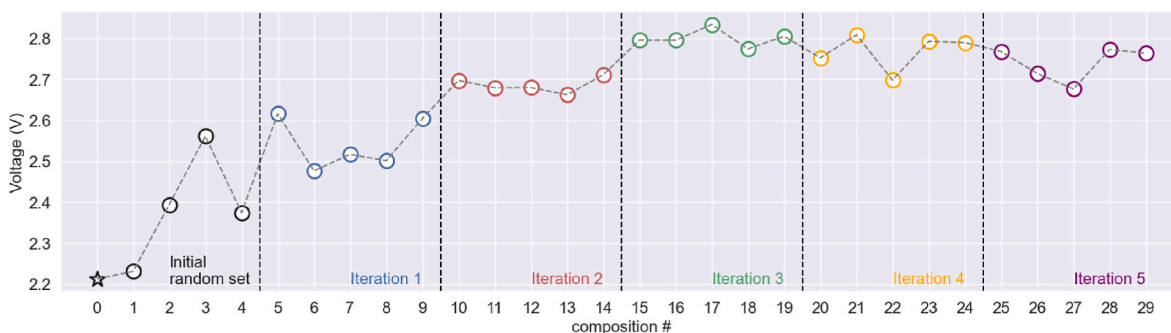


Fig. 2. Bayesian optimization-guided average voltage for conversion reactions, obtained from DFT calculations. The compositions were identified using BO based on GPR models.

average value over the four configurations. However, the standard deviation in the energy above hull was $\sim 20\%$ of the average value for the equimolar alloys. Hence, the conversion reaction voltage was chosen as the target property in this study, followed by evaluations of the thermodynamic stability and electronic structure.

The reference composition in this study was the equimolar $(\text{Fe}_{0.2}\text{Cu}_{0.2}\text{Zn}_{0.2}\text{Mn}_{0.2}\text{Mg}_{0.2})\text{F}_2$. Henceforth, this equimolar composition was denoted as HEF-44444. The sequence of elements in the numerical indices was Fe, Cu, Zn, Mn, and Mg. As seen in Fig. 2, the conversion voltage for this equimolar composition was 2.21 V (denoted by the black star symbol at index 0). Our initial dataset consisted of 4 randomly chosen fluoride alloy compositions (denoted by the 4 black circles in Fig. 2, composition #1–4) that have calculated voltages between 2.23 V and 2.56 V, with a mean value ~ 2.39 V. Composition #1 was $(\text{Fe}_{0.3}\text{Cu}_{0.1}\text{Zn}_{0.2}\text{Mn}_{0.3}\text{Mg}_{0.1})\text{F}_2$ and was denoted as HEF-62462 following the convention mentioned above for the equimolar alloy. HEF-62462 contained 30 % Mn and Fe each and had the lowest voltage. Composition #3 (HEF-66422) contained 30 % Cu and Fe each. The randomly chosen 4 datapoints were used to train a Gaussian Process Regression (GPR) model. In the first iteration, five most promising candidate chemistries with the best expected improvement in conversion voltage were selected for further DFT calculations. The mean DFT-computed voltage for these chemistries (compositions #5–9) was ~ 2.54 V, which was a 0.15 V increase compared to the mean value of randomly selected chemistries (compositions #1–4). The combined amount of Fe, Cu, and Zn in these compositions selected in the first iteration was 75–85 %, with nearly equal amounts for each element. Mn and Mg were present in smaller amounts. The exact compositions are provided in Table S2 of the SI. For the second iteration, samples indexed 1–9 were used to train a GPR model and the top five candidates were extracted for further DFT calculations (shown using red circle markers for composition #10–14). A total of 5 iterations were implemented to generate DFT-

data for 29 unique chemistries in addition to the starting equimolar alloy.

The voltage distribution across the 5 iterations and the initial set is shown in Fig. 3(a). The initial random set includes compositions #1–4. The equimolar fluoride was used as the reference baseline chemistry. The mean value within each iteration were found to increase steadily until iteration 3, which had a mean voltage of 2.80 V. Composition #17, $(\text{Fe}_{0.1}\text{Cu}_{0.4}\text{Zn}_{0.4}\text{Mg}_{0.05}\text{Mn}_{0.05})\text{F}_2$, denoted as HEF-28811 had the highest voltage of 2.83 V amongst these 30 compositions. This was 28 % larger than the voltage of the equimolar HEF-44444. All compositions in iteration 3 contained 40 % Cu, at least 25 % Zn, and $\sim 50\%$ Zn and Fe combined. The mean voltage in iteration 4 (#20–24) dropped slightly to 2.77 V. Since the previous iterations already identified compositions with the highest voltages, successive iterations extracted the next-best HEF compositions and resulted in decrease in the mean voltage within that set of compositions. All compositions in iteration 4 contained 30–40 % Cu and 30–40 % of either Fe or Zn. Compositions in iteration 5 (#25–29) had similar chemistries and voltage as those in iteration 4, with a mean voltage of 2.74 V. Composition-voltage data for all 30 fluorides across five iterations is given in Table S2 of the SI.

While Bayesian optimization was used to extract cathode chemistries with high conversion voltages, it is of interest to create a general model that provides the conversion voltage of any cathode chemistry as a function of its composition. Therefore, data generated using DFT calculations was used to build predictive models. For the simplest model, the conversion voltage was directly predicted using a composition weighted average (known commonly as the rule of mixtures). This model does not employ additional structural, chemical, or electronic features except the chemical composition of the fluoride alloy and calculated conversion voltages for the binary fluorides provided in Fig. 1 and in Table S1 of the SI Fig. 3(b) shows the parity between the voltages from DFT and ‘rule of mixtures (ROM)’ predictions. The equimolar

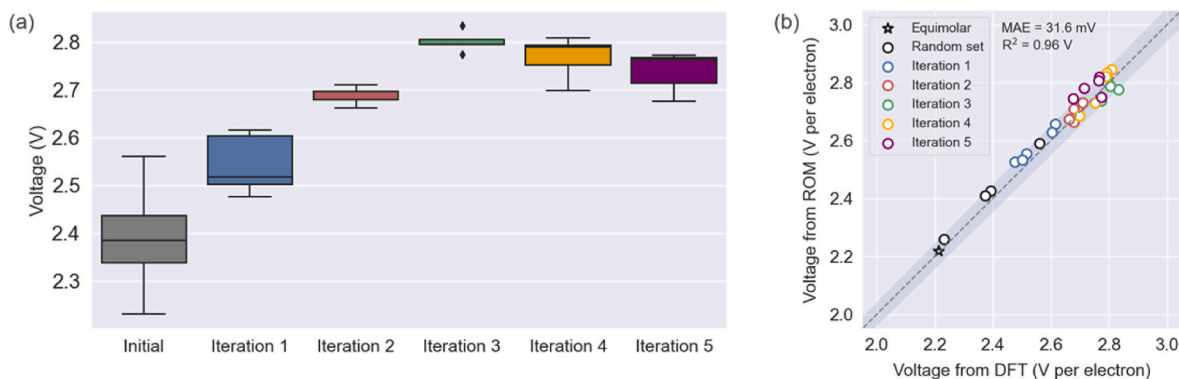


Fig. 3. (a) Box plots showing the distribution of DFT-computed voltages for candidates discovered in each iteration of the Bayesian optimization process. (b) Parity plot between conversion voltage (per electron transfer) calculated using DFT calculations and composition-weighted linear interpolation using the rule of mixtures. The shaded patch shows the 2.5 % error window.

composition (black star marker) lies very close to the parity line (diagonal gray dashed line). 29 out of the 30 HEF compositions have relative errors between the voltage values less than 2.5 %; and lie within the shaded gray patch. Overall, the ROM model yielded a mean absolute error (MAE) of 31.6 mV, root mean squared error (RMSE) of 35.42 mV, and R^2 value of 0.96. These results indicate that the simple ROM models are reasonably accurate, suggesting no prominent synergistic effects of high-entropy systems on the conversion voltages. Thus, the average voltage of the multi-element fluoride cathode could be determined by the voltages of its constituent binary fluorides.

Having established this computationally affordable model, the ROM was directly used to predict compositions with the maximum voltage (amongst the 2226 compositions in our search space) to assess the quality of our search protocols. From the results in Fig. 2, seven compositions (#15, 16, 17, 19, 21, 23, 24 whose notations are HEF-58511, HEF-48611, HEF-28811, HEF-38711, HEF-88211, HEF-78311, HEF-68411 respectively) have DFT voltages between 2.78 V and 2.84 V, which is within 2 % of the maximum prediction from ROM and also a >25 % increase compared to the voltage of the equimolar composition #0 (HEF-44444). These seven compositions contain 40 % Cu and 50 % Fe and Zn combined. It was expected based on the ROM model since CuF_2 and FeF_2 have the highest conversion reaction voltages, and MnF_2 and MgF_2 have the lowest conversion reaction voltages. The concentration of Mg and Mn is 5 % each, which is the minimum permitted value in our search space. These results verified that our Bayesian Optimization procedure can identify the best candidates with high voltages in few iterations, since it achieved essentially the same results as a direct prediction.

2.2. Thermodynamic stability

The free energy of these alloys at 300 K was calculated using the DFT-derived enthalpy at 0 K and configurational entropy due to disorder at the M cationic site. Results in Fig. 4 show that many alloys (16 out of 30) have enthalpies above hull by less than 10 meV/atom. The convex energy hull was composed of the five binary fluorides in the rutile phase. Upon adding the configurational entropy contributions computed as $-k_B T \sum_i p_i \ln(p_i)$ where k_B is the Boltzmann constant, T is the temperature in K and p_i is the elemental fraction, all of the alloyed fluorides have $\Delta G < 0$ at 300 K, indicating thermodynamic stability relative to the mixture of the five binary fluorides. While vibrational entropy calculations were not done for the compositions studied here, our previous work showed that the contribution of vibrational entropy to the free energy of equimolar $(\text{Fe}_{0.2}\text{Cu}_{0.2}\text{Zn}_{0.2}\text{Ni}_{0.2}\text{Co}_{0.2})\text{F}_2$ was 14.1 meV/atom at 300 K, which was 33 % of the value of the contribution from configurational entropy at 300 K as also calculated for equimolar alloys in our previous work. This can further reduce the free energy at room temperature and decrease the mixing temperature to improve

synthesizability.

2.3. Experimental validation

We performed structural and electrochemical characterization to validate the findings reported in earlier sections. The equimolar fluoride (#0: HEF-44444), four fluoride compositions in the initial random set (#1–4), and two high voltage fluorides identified using BO (#16: HEF-48611 and #17: HEF-28811) were synthesized using high-energy ball milling as described in detail at the Experimental Section. As indicated in X-ray diffraction shown in Fig. 5(a), single phase rutile-structured metal fluorides were successfully synthesized with no evidence of phase segregation, consistent with thermodynamic free energy calculations shown earlier in Fig. 4. Fig. 5(b) shows galvanostatic discharge-charge voltage profiles of the selected compositions. The voltage profiles for the rest are provided in Fig. S3 of the SI. To maintain consistency with the conversion voltages of binary fluorides reported earlier in Fig. 1 (a), the voltage of HEF cathodes was calculated using two protocols: (i) at a specific capacity of 50 mAh/g which was indicated using vertical gray lines in Fig. 5(b) and (ii) average value of the peaks in the differential capacity vs voltage profile as all samples were found to have two dQ/dV maxima (Figs. S3(c) and S4(a) of the SI). The equimolar composition #0 (HEF-44444, black-colored) had an experimental conversion voltage of 2.23 V at a specific capacity of 50 mAh/g, while the compositions #16 (HEF-48611, blue-colored) and #17 (HEF-28811, red-colored) showed experimental conversion voltages of 2.58 V and 2.57 V at 50 mAh/g, respectively. For these three compositions, the average voltages from the dQ/dV peaks were 2.20 V, 2.60 V, and 2.59 V, respectively. The stars in Fig. 5(c) indicate the voltage value at the specific dQ/dV peaks. Using both calculation protocols, compositions #16 (HEF-48611) and #17 (HEF-28811) had 15–18 % larger experimental voltage compared to the equimolar HEF-44444. Since compositions #16 and #17 contain 40 % Cu, it is likely that the first plateau at specific capacities up to 50 mAh/g was arising from the conversion of predominantly Cu from the rutile phase to the metallic phase. The second voltage plateau likely originated from the participation of Fe and Zn in the conversion reaction.

For reference, Fig. 5(c) shows the comparison between DFT-computed conversion reaction voltages (blue bars) and experimental ones obtained from galvanostatic discharge-charge measurements. The DFT-computed voltages of compositions #16 (HEF-48611) and #17 (HEF-28811) were 26 % and 28 % larger than the DFT-computed voltage of the equimolar composition #0 (HEF-44444). We found that the DFT voltage was consistently larger than the experimental voltage.

Fig. 5(d) shows the cycling stability of composition #16 and #17 which retained a capacity of almost 124 mAh/g and 156 mAh/g respectively after 50 cycles. In contrast, the capacity of the equimolar alloy (HEF-44444) degrades to 33 mAh/g after 50 cycles. Fig. 5(d) also

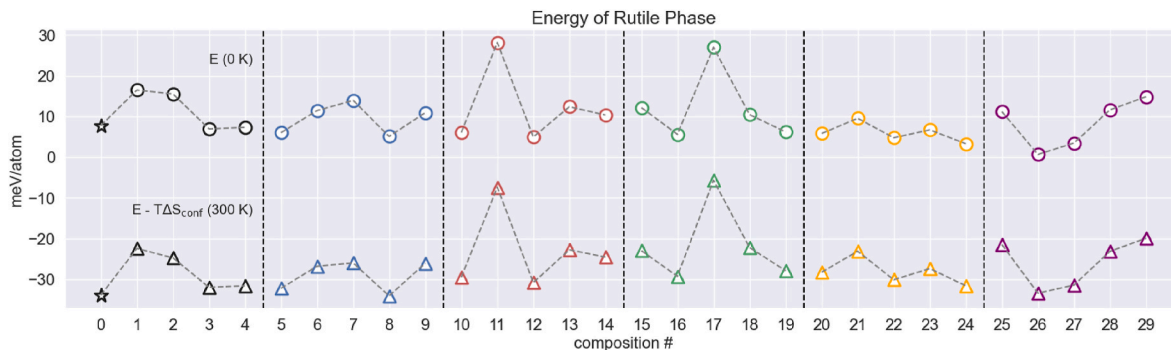


Fig. 4. Thermodynamic stability of multi-element fluorides at room temperature computed using the DFT enthalpy at 0 K (relative to the energies of the binary fluorides) and configurational entropy contributions. Circular markers denote the enthalpy at 0 K. Triangular markers denote the free energy at 300 K, computed by adding the configurational entropy contributions.

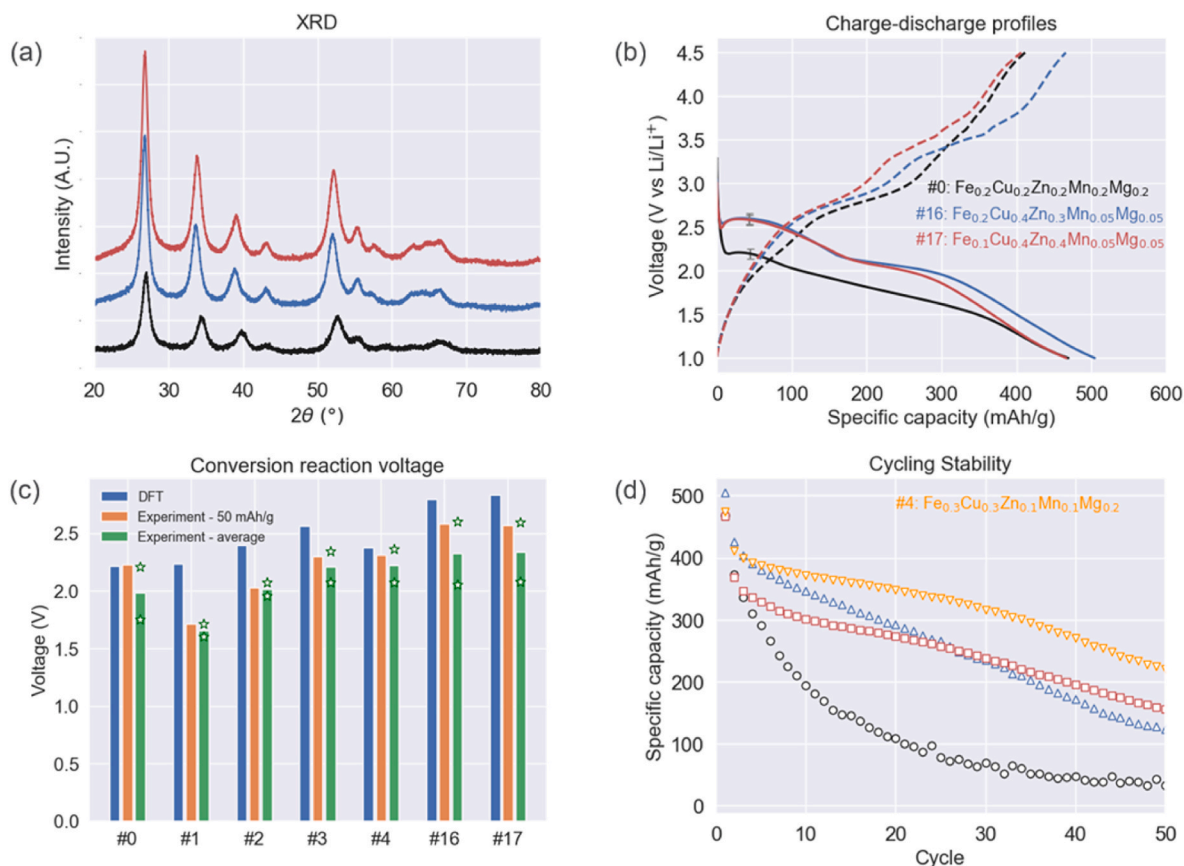


Fig. 5. Experimental results for few cathode chemistries screened in this work. (a) XRD spectra for compositions #0 (HEF-44444), #16 (HEF-48611), and #17 (HEF-28811), (b) 1st charge-discharge profile for compositions #0, #16, and #17. The vertical gray bars are at 50 mAh/g. Additional charge-discharge profiles are given in Fig. S6. (c) DFT-computed and experimentally measured voltages. The orange bars denote voltage values from the 1st discharge at a specific capacity of 50 mAh/g and the green bars denote the average of the dQ/dV peaks from the differential capacitance profile; which is shown in Fig. S4 of the SI. The stars on (c) denote the voltage of the two peaks in the dQ/dV profile. (d) Cycling data for compositions #0 (HEF-44444), #16 (HEF-48611), #17 (HEF-28811), and #4 (HEF-66224). (For interpretation of the references to color in this figure legend, the reader is referred to the Web version of this article.)

includes data for composition #4 (HEF-66224), which had a specific capacity of 220 mAh/g after 50 cycles (in spite of a lower experimental voltage of 2.24 V). Possible reasons for capacity degradation include the repeated splitting and restructuring of the alloys during lithiation/delithiation, interfacial side reactions and the dissolution of transition metal ions during cycling. To put these findings in perspective, recent studies on equimolar $(\text{FeCuZnNiCo})\text{F}_2$ showed a capacity of ~ 140 mAh/g after 50 cycles [12]. Our Bayesian optimization-guided experimental results demonstrated a better capacity for non-equimolar 5-element fluorides in the Fe-Cu-Zn-Mn-Mg space which does not contain high toxicity elements such as Ni and Co. The same work also reported an increased capacity of ~ 210 mAh/g for equimolar $(\text{FeCuZnNiCoMnMg})\text{F}_2$, which showed the promising impact of Mn and Mg on cycling stability and entropy stabilization with higher configurational entropy [12]. Promising approaches to achieve outstanding cycle stability using fluoride/carbon nanocomposites were demonstrated in multicore-shell $\text{FeF}_3@C/\text{Li}$ cells [28] and metal-organic framework derived CoF_2 nanoconfinement [29]. Additional voltage profiles, XRD spectra, and cycling stability for compositions #1–3 are shown in Fig. S3 of the SI. These compositions also demonstrated stability of the rutile phase and capacity retention up to 115 mAh/g after 50 cycles.

3. Discussion

Seeing the reasonable agreement between voltages calculated using DFT and ROM, the ROM model was used to predict the voltages of all the 2226 compositions in our search space. We note that ROM did not give

the true DFT values, but it was used as an approximation since the error metrics were small: $\text{MAE} = 31.6$ mV and $R^2 = 0.96$. The composition with the highest voltage using ROM was $(\text{Fe}_{0.4}\text{Cu}_{0.4}\text{Zn}_{0.1}\text{Mn}_{0.05}\text{Mg}_{0.05})\text{F}_2$, with a value of 2.84 V. From Fig. 2, this composition was identified using BO in iteration 4 (composition #21: HEF-88211) and had a DFT voltage of 2.81 V. Overall, by sampling less than 1.5 % of the total search space, we identified several cathode chemistries with voltages close to the estimated maximum value (estimated using ROM, which was considered as a good approximation of the DFT calculated voltage). We note that it was not known a priori whether multicomponent fluorides can have voltages significantly higher than the linear composition-weighted average of the constituent binary fluorides. The good agreement between ROM and DFT voltages suggests that ROM can be used as a quick yet accurate model to predict the average conversion reaction voltage. Overall, amongst the 29 explored non-equimolar HEF-alloys, seven had conversion voltages greater than 2.78 V, which was a >25 % increase compared to the voltage of the equimolar alloy (2.21 V). We also evaluated the accuracy of ROM-based calculations for experimental conversion reaction voltages reported in Fig. 5(c). Since Mg is electrochemically inactive above 1 V relative to Li/Li^+ , the HEF compositions were rescaled such that the molar fractions of Fe, Cu, Zn, and Mn sum up to 1. Data in Fig. S5 of the SI shows a reasonable fit with a mean absolute error of 0.1 V.

While the compositions identified using our BO-guided search are (i) predominantly Fe and Cu rich and (ii) limited to a maximum molar fraction of 0.4 to ensure entropic effects, a robust ROM model should also yield good results for other compositions in this Fe-Cu-Zn-Mn-Mg

chemical space. Therefore, in addition to the results presented in Fig. 2, voltages of few other compositions were also calculated using DFT to test the accuracy of the ROM. Results in Table S3 of the SI show good agreement between the DFT and ROM voltages, demonstrating the validity of the ROM models or suppression of synergistic high-entropy effects on the conversion voltage. We report good agreement between DFT and ROM for compositions containing up to 0.4 mol fraction of Mn and other compositions containing up to 0.6 mol fraction of Cu. It is however noted that higher amounts of Cu (or any one element) will reduce the entropic contribution to the thermodynamic stability and may result in poor cycling characteristics due to agglomeration effects [7].

Another important requirement for cathodes is small bandgaps for easy electron conduction. The total electronic density of states (DOS) of the seven compositions with DFT-computed average voltage greater than 2.78 V is shown in Fig. 6(a). All compositions were identified in iterations 3 and 4 and their DOS plots are colored accordingly. They have direct bandgaps ranging from 0.3 eV to 0.83 eV calculated at the GGA + U level of theory. The bandgap here is the energy gap between the valence band maximum and the lowest unoccupied electronic state, which has also been characterized as impurity/defect states in the literature for similar HEF cathodes [12]. For reference, Fig. S7 in the SI includes DOS plots for ZnF_2 , which is a binary fluoride and has a larger bandgap of 3.2 eV. However, the bandgap was reduced in multi-element fluorides. It is shown from the orbital resolved DOS plot in Fig. 6(b) that for composition #15 (HEF-58511), the top valence bands were primarily originating from the partially occupied Fe-3d and Mn-3d states. The deeper valence bands have strong contributions from Cu-3d and Zn-3d states, with weak contributions from Fe-3d and Mn-3d states, corresponding to their respective fractions in the alloys. The bottom conduction band at 0.3–1.1 eV above Fermi level was made of Cu-3d states. The top valence band in composition #17 (HEF-28811) is also predominantly of Fe-3d character. Lower Fe content resulted in weaker Fe-3d intensity compared to composition #15 (HEF-58511). The deeper valence bands were primarily originating from Cu-3d and Zn-3d states. The Mn-3d states occupied the same energy interval as in composition #15. The conduction band or impurity band states 0.8 eV above the Fermi level was predominantly composed of Cu-3d states. In both cases, the Mg-2p, Cu-4s, and Zn-4s states have much lower DOS intensities relative to the other elements (see Fig. S8) and contribute to the top valence band and the bottom conduction band insignificantly.

High entropy alloys or high-entropy ceramics are the materials of interest here since cationic disorder can potentially lead to improved electrochemical properties and thermodynamic stability. While

equimolar alloys have the highest contribution of configurational entropy, non-equimolar alloys are demonstrated to considerably expand search space for the property of interest. Fig. 4 shows that the configurational entropy for all alloys discovered here varies within a relatively narrow range, with values lying between 32 meV and 42 meV (the upper limit is the equimolar alloy). Increasing the composition of the major element reduces the configurational entropy, thereby reducing the alloy stability. Hence, the maximum contribution of any element to an alloy composition in our study was limited to 0.4, which limits the decrease of configurational entropy to less than 25 %. The configurational entropy of each fluoride composition is given Table S2 in the SI. On the other hand, electrochemical properties and performance can potentially be enhanced for non-equimolar compositions. This is evident from the greater cycling stability of the three non-equimolar fluorides presented in Fig. 5(d).

We compared the theoretical voltages for the high-entropy fluorides with the dQ/dV peak positions obtained from experimental first discharge profiles and at a fixed specific capacity of 50 mAh/g. As shown in Fig. 5(c), computational voltages are mostly found to be larger than the experimental voltages. One possible reason for this overestimation from DFT calculations is size-dependent effects. All DFT calculations in this work assume a perfect bulk configuration for the fluoride and metallic phases. However, recent size-dependent calculations showed that the theoretical voltages for CuF_2 , NiF_2 and FeF_2 were reduced by up to 0.6 V by considering subnanometer size metallic clusters [26]. Experimental observed agglomeration during CuF_2 to Cu conversion can lead to significantly lower experimental voltages for the binary fluorides [7], compared to the DFT-computed average voltage. Additionally, the presence of more than one voltage plateau in the charge-discharge profiles points towards the selective conversion of elements with high electrochemical activity relative to Li/Li^+ , which could also lead to localized clustering within the alloyed fluoride during cycling. The diffusivity of the different elements in the rutile structure can also impact the cycling stability of these cathodes and needs to be examined in detail. Other research directions in this field can include multi-property Bayesian optimization approaches to simultaneously maximize the conversion voltage, decrease the bandgap, and enhance cycling stability.

4. Methods/Experimental Section

4.1. Special Quasirandom Structure (SQS)

The SQS supercells were generated using the Alloy Theoretic

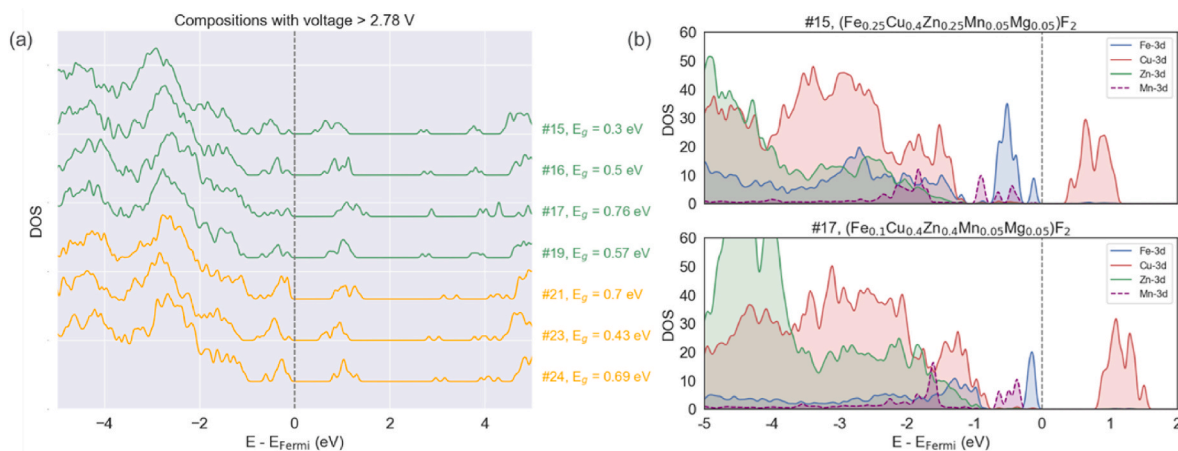


Fig. 6. Electronic density of states (DOS) for HEF compositions with voltage greater than 2.78 V calculated at the GGA + U level of theory. (a) Total DOS (arbitrary units) and band gaps for the compositions. The vertical dashed gray line at 0 denotes the Fermi level. The color code for each composition indicates the iteration within which it was identified. (b) Orbital resolved DOS (arbitrary units) for composition #15 and composition #17. (For interpretation of the references to color in this figure legend, the reader is referred to the Web version of this article.)

Automated Toolkit (ATAT) [30], in which a Monte Carlo-based evolutionary algorithm was used to search the periodic atomic structure with the closest match of correlation functions of an ideally mixed solid-solution state. The configurations were generated using the ATAT code [30]. The schematics in Fig. 1 are generated using VESTA [31].

4.2. Density Functional Theory (DFT)

All calculations were performed using the Vienna Ab initio Simulation Package (VASP) [32,33], implemented using the generalized gradient approximation (GGA) for exchange-correlation functionals [34]. The Perdew–Burke–Ernzerhof (PBE) exchange–correlation functional with the projector augmented–wave method [35] and 500 eV plane–wave energy cutoff were used for all the calculations. The multi-element fluoride phases were modeled using a $2 \times 2 \times 5$ rutile supercell with 120 atoms and a single Γ -centred k-point. Defluorinated multi-element metallic phases were modeled using a $3 \times 4 \times 5$ body-centred cubic (BCC) supercell with 120 atoms and a $2 \times 1 \times 1$ k-point mesh. Li and Fe metals were modeled as BCC phases with 2 atoms in the conventional unit cell. Mn metal was modeled as α -Mn, which is based on a BCC Bravais lattice with a 29 atom bases. Mg and Zn were modeled as hexagonal close packed (HCP) phases with 2 atoms per conventional cell. Cu was modeled as a conventional face-centred cubic (FCC) phase with 4 atoms per cell. LiF was modeled as a conventional FCC phase. For GGA + U calculations, the Hubbard effective on-site energies are used in the formalism of Dudarev [36]. The on-site repulsion Hubbard parameters for Fe, Cu, and Mn are 5.30, 4.00, and 3.90 eV respectively, as published in the Materials Project [27,37].

4.3. Bayesian Optimization (BO)

Here, we used Gaussian Process Regression (GPR) [38] models with the Matérn kernel with the smoothness parameter (ν) equal to 1.5 by utilizing GPyTorch package [39]. ‘Expected Improvement (EI)’ is the acquisition function used here and is described in Equations (3)–(6).

$$EI(x) = \begin{cases} (\mu(x) - f(x^*) - \epsilon)\Phi(Z) + \sigma(x)\psi(Z), & \text{if } \sigma(x) > 0 \\ 0, & \sigma(x) = 0 \end{cases} \quad \text{Equation 3}$$

$$\Phi(Z) = \frac{1}{\sqrt{2\pi}} \int_{-\infty}^Z e^{-\frac{t^2}{2}} dt \quad \text{Equation 4}$$

$$\psi(Z) = \frac{e^{-\frac{Z^2}{2}}}{\sqrt{2\pi}} \quad \text{Equation 5}$$

$$Z = \frac{\mu(x) - f(x^*) - \epsilon}{\sigma(x)} \quad \text{Equation 6}$$

where $\mu(x)$ and $\sigma(x)$ are the mean and standard deviation for the testing dataset x predicted using GPR. $f(x^*)$ is the optimal property value (maximum voltage in this case) in the training dataset x^* , $\Phi(Z)$ and $\psi(Z)$ are the cumulative – density function and probability – density function, respectively, the variable Z is defined in Equation 6, and the parameter ϵ determines the extent of exploration during the optimization procedure. Since the initial model training procedure is done with only 4 compositions, our feature set only includes (i) element fraction, (ii) transition metal fraction, (iii) band centre of the fluoride composition, and (iv) band centre of the metallic composition, calculated using the matminer library [40].

4.4. Material preparation and characterization

Multi-cation fluorides investigated in this study were synthesized by a mechanochemical method using high-energy ball milling. Binary

fluorides (FeF_2 , CuF_2 , ZnF_2 , MnF_2 , MgF_2) were mixed in a mortar first, transferred to a stainless-steel jar with stainless-steel balls, and ball-milled for 3 h using SPEX Mill 3000. Then, the synthesized powders were mixed with carbon black (C45, Timcal) and additionally ball-milled for 3 h to make metal fluoride–carbon nanocomposite [41]. Each individual metal fluoride–carbon nanocomposites were prepared under the same condition. Electrodes were prepared by slurry casting method, with the ink consisted of 85 wt% of active material, 5 wt% carbon black and 10 wt% polyvinylidene fluoride (PVDF) in N-methyl-2-pyrrolidone, on Al foil. The electrode films were dried overnight at 110 °C in a vacuum. All procedures were performed in Ar-filled glove box to minimize air/moisture exposure. X-ray diffraction (XRD) patterns of metal fluoride–carbon nanocomposite powders were measured using Rigaku Miniflex with $\text{CuK}\alpha$ radiation source (1.5406 Å). Electrochemical coin cell testing was conducted using the 2032 coin cell configuration. The coin cells were composed of metal fluoride–carbon nanocomposite cathode, GF/F glass fiber separator (Whatman), and Li metal anode (MTI corporation). 1.2 M LiPF_6 in EC/EMC (3:7 wt ratio) was used as an electrolyte. Battery cycling test was performed using Maccor battery cycler (Maccor). A current density of 50 mA/g was applied between 1.0 V and 4.5 V for each cycle at 30 °C.

5. Conclusions

Bayesian optimization-based computational exploration of Co and Ni free non-equi-molar ($\text{Fe}_{x1}\text{Cu}_{x2}\text{Zn}_{x3}\text{Mn}_{x4}\text{Mg}_{x5}$) F_2 fluorides resulted in the efficient screening of high voltage chemistries by sampling less than 1.5 % of the chemical search space. Compounds rich in Fe, Cu, and Zn (70–80 % mole percent combined) demonstrated up to 28 % conversion reaction voltage relative to the equimolar composition. Even in these multi-element fluorides, the rule of mixtures was found to be a good approximation for the computational conversion reaction voltage, which was corroborated by observed experimental trend. Electronic structure calculations at the GGA + U level of theory revealed much smaller energy gaps in multi-element fluorides compared to their single-element counterparts owing to new electronic states arising from compositional disorder, which is promising for improving electronic conductivity in these cathodes. Several non-equi-molar chemistries were synthesized experimentally and showed single-phase stability and improved conversion voltage relative to the equimolar composition. Some of these chemistries had better cycling performance than previously reported multi element compositions, which included Ni and Co, pointing to further opportunities in discovery of high entropy cathodes for sustainable batteries.

CRedit authorship contribution statement

Aditya Sundar: Writing – review & editing, Writing – original draft, Resources, Methodology, Investigation, Data curation, Conceptualization. **Jehee Park:** Writing – review & editing, Writing – original draft, Investigation, Data curation. **Haesun Park:** Writing – review & editing, Methodology. **Eungje Lee:** Writing – review & editing, Supervision, Conceptualization. **Jae Jin Kim:** Writing – review & editing, Supervision, Project administration, Methodology, Investigation, Funding acquisition. **Peter Zapol:** Writing – review & editing, Supervision, Resources, Investigation, Conceptualization.

Declaration of competing interest

The authors declare that they have no known competing financial interests or personal relationships that could have appeared to influence the work reported in this paper.

Acknowledgements

The work is performed using Laboratory Directed Research and

Development (LDRD) funding from Argonne National Laboratory, provided by the Director, Office of Science, of the United States Department of Energy under Contract No. DE-AC02-06CH11357. We gratefully acknowledge the computing resources provided on Bebop, a high-performance computing cluster operated by the Laboratory Computing Resource Center at Argonne National Laboratory.

Appendix A. Supplementary data

Supplementary data to this article can be found online at <https://doi.org/10.1016/j.jpowsour.2025.236448>.

Data availability

Data will be made available on request.

References

- [1] F. Wu, G. Yushin, Conversion cathodes for rechargeable lithium and lithium-ion batteries, *Energy Environ. Sci.* 10 (2017) 435–459.
- [2] F. Wang, et al., Conversion reaction mechanisms in lithium ion batteries: study of the binary metal fluoride electrodes, *J. Am. Chem. Soc.* 133 (2011) 18828–18836.
- [3] S.-H. Yu, X. Feng, N. Zhang, J. Seok, H.D. Abruna, Understanding conversion-type electrodes for lithium rechargeable batteries, *Acc. Chem. Res.* 51 (2018) 273–281.
- [4] X. Hua, et al., Revisiting metal fluorides as lithium-ion battery cathodes, *Nat. Mater.* 20 (2021) 841–850.
- [5] X. Zhao, Z. Zhao-Karger, M. Fichtner, X. Shen, Halide-based materials and chemistry for rechargeable batteries, *Angew. Chem. Int. Ed.* 59 (2020) 5902–5949.
- [6] L. Sun, Y. Li, W. Feng, Metal fluoride cathode materials for lithium rechargeable batteries: focus on iron fluorides, *Small Methods* 7 (2023) 2201152.
- [7] X. Hua, et al., Comprehensive study of the CuF_2 conversion reaction mechanism in a lithium ion battery, *J. Phys. Chem. C* 118 (2014) 15169–15184.
- [8] A. Sarkar, et al., High entropy oxides for reversible energy storage, *Nat. Commun.* 9 (2018) 3400.
- [9] J.W. Sturman, E.A. Baranova, Y. Abu-Lebdeh, Review: high-entropy materials for lithium-ion battery electrodes, *Front. Energy Res.* 10 (2022).
- [10] Y.F. Ye, Q. Wang, J. Lu, C.T. Liu, Y. Yang, High-entropy alloy: challenges and prospects, *Mater. Today* 19 (2016) 349–362.
- [11] E.P. George, D. Raabe, R.O. Ritchie, High-entropy alloys, *Nat. Rev. Mater.* 4 (2019) 515–534.
- [12] Y. Cui, et al., High entropy fluorides as conversion cathodes with tailorable electrochemical performance, *J. Energy Chem.* 72 (2022) 342–351.
- [13] F. Wang, et al., Ternary metal fluorides as high-energy cathodes with low cycling hysteresis, *Nat. Commun.* 6 (2015) 6668.
- [14] C. Villa, S. Kim, Y. Lu, V.P. Dravid, J. Wu, Cu-substituted NiF_2 as a cathode material for Li-ion batteries, *ACS Appl. Mater. Interfaces* 11 (2019) 647–654.
- [15] Y. Zhang, D.W. Apley, W. Chen, Bayesian optimization for materials design with mixed quantitative and qualitative variables, *Sci. Rep.* 10 (2020) 4924.
- [16] T. Morishita, H. Kaneko, Initial sample selection in bayesian optimization for combinatorial optimization of chemical compounds, *ACS Omega* 8 (2023) 2001–2009.
- [17] Y. Zuo, et al., Accelerating materials discovery with Bayesian optimization and graph deep learning, *Mater. Today* 51 (2021) 126–135.
- [18] A. Talapatra, et al., Autonomous efficient experiment design for materials discovery with Bayesian model averaging, *Phys. Rev. Mater.* 2 (2018) 113803.
- [19] M. Ohashi, S. Maeda, C. Sato, Helical three dimensional reconstruction using bayesian optimization for cryogenic electron microscopy, *IEEE ACM Trans. Comput. Biol. Bioinf* (2023) 1–12, <https://doi.org/10.1109/TCBB.2023.3268793>.
- [20] F. Hildenbrand, F. Aupperle, G. Stahl, E. Figgmeier, D.U. Sauer, Selection of electrolyte additive quantities for lithium-ion batteries using bayesian optimization, *Batter. Supercaps* 5 (2022).
- [21] G. Dogan, et al., Bayesian machine learning for efficient minimization of defects in ALD passivation layers, *ACS Appl. Mater. Interfaces* 13 (2021) 54503–54515.
- [22] J.K. Pedersen, et al., Bayesian optimization of high-entropy alloy compositions for electrocatalytic oxygen reduction, *Angew. Chem. Int. Ed.* 60 (2021) 24144–24152.
- [23] V.A. Mints, et al., Exploring the composition space of high-entropy alloy nanoparticles for the electrocatalytic H_2/CO oxidation with bayesian optimization, *ACS Catal.* 12 (2022) 11263–11271.
- [24] D. Khatamsaz, et al., Bayesian optimization with active learning of design constraints using an entropy-based approach, *npj Comput. Mater.* 9 (2023) 49.
- [25] R. Jalem, et al., Bayesian-driven first-principles calculations for accelerating exploration of fast ion conductors for rechargeable battery application, *Sci. Rep.* 8 (2018) 5845.
- [26] J.K. Seo, et al., Revisiting the conversion reaction voltage and the reversibility of the CuF_2 electrode in Li-ion batteries, *Nano Res.* 10 (2017) 4232–4244.
- [27] A. Jain, et al., Formation enthalpies by mixing GGA and GGA + U calculations, *Phys. Rev. B* 84 (2011) 045115.
- [28] Z. Jiang, et al., Multicore-shell iron fluoride@carbon microspheres as a long-life cathode for high-energy lithium batteries, *J. Mater. Chem. A Mater.* 11 (2023) 21541–21552.
- [29] F. Wu, et al., Metal-organic framework-derived nanoconfinements of CoF_2 and mixed-conducting wiring for high-performance metal fluoride-lithium battery, *ACS Nano* 15 (2021) 1509–1518.
- [30] A. van de Walle, et al., Efficient stochastic generation of special quasirandom structures, *Calphad* 42 (2013) 13–18.
- [31] K. Momma, F. Izumi, VESTA: a three-dimensional visualization system for electronic and structural analysis, *J. Appl. Crystallogr.* 41 (2008).
- [32] G. Kresse, J. Hafner, Ab initio molecular dynamics for liquid metals, *Phys. Rev. B* 47 (1993).
- [33] G.a Kresse, D.b. Joubert, From ultrasoft pseudopotentials to the projector augmented-wave method, *Phys. Rev. B Condens. Matter* 59 (1999).
- [34] J.P. Perdew, K. Burke, M. Ernzerhof, Generalized gradient approximation made simple, *Phys. Rev. Lett.* 77 (1996).
- [35] P.E. Blöchl, Projector augmented-wave method, *Phys. Rev. B* 50 (1994).
- [36] S. Dudarev, G. Botton, Electron-energy-loss spectra and the structural stability of nickel oxide: an LSDA+ U study, *Phys. Rev. B Condens. Matter* 57 (1998).
- [37] A. Jain, et al., Commentary: the Materials Project: a materials genome approach to accelerating materials innovation, *Apl. Mater.* 1 (2013) 011002.
- [38] V.L. Deringer, et al., Gaussian process regression for materials and molecules, *Chem. Rev.* 121 (2021) 10073–10141.
- [39] J.R. Gardner, G. Pleiss, D. Bindel, K.Q. Weinberger, A.G. Wilson, GPyTorch: Blackbox Matrix-Matrix Gaussian Process Inference with GPU Acceleration, 2018.
- [40] L. Ward, et al., Matminer: an open source toolkit for materials data mining, *Comput. Mater. Sci.* 152 (2018) 60–69.
- [41] F. Wang, et al., Conversion reaction mechanisms in lithium ion batteries: study of the binary metal fluoride electrodes, *J. Am. Chem. Soc.* 133 (2011) 18828–18836.